Polarization effects in 3D vectorial induced current reconstructions

Christelle Eyraud, Rodolphe Vaillon, Amelie Litman, Jean-Michel Geffrin, Olivier Merchiers

Polarization effects in 3D vectorial induced current reconstructions

Christelle Eyraud,[1,*] Rodolphe Vaillon,[2] and Amélie Litman[1], Jean-Michel Geffrin[1], Olivier Merchiers[3]

[1] *Aix Marseille Université, CNRS, Centrale Marseille, Institut Fresnel, UMR 7249, 13013 Marseille, France*

[2] *Université de Lyon, CNRS, INSA-Lyon, UCBL, CETHIL, UMR5008, F-69621, Villeurbanne, France*

[3] *Université de Bordeaux, CRPP-UPR CNRS 8641, 33600 Pessac, France*

compiled: June 10, 2018

In tomography algorithms, the complex amplitude scattering matrix corresponds to the input parameter. When considering three-dimensional targets, the scattering matrix is now containing vectorial information. Thus, this scattering matrix might be calculated with various polarization projections. Moreover, when dealing with experimental data, we are almost every time faced with truncated data. We focus here on the impact of selecting parts of the amplitude scattering matrix elements versus others and in particular on the influence of the polarization choices on the imaging results. In order to better apprehend the physical content associated to each polarization term, the study is conducted with a simple vectorial induced current reconstruction algorithm allowing to reconstructed qualitative maps of the scene. This algorithm is applied on scaled models of aggregates combined with experimental scattered fields acquired in the microwave frequency range.

1. Introduction

Electromagnetic wave probing is an interesting tool to obtain the physical features of unknown targets (position, shape, size, complex permittivity). Indeed, these characteristics can be retrieved from the measurements of its scattered field by an inverse procedure. In practice, there exists some difficulties in particular when dealing with measurements. Indeed, as the scattered field can not be measured on an entire surface enclosing the target - due to mechanical constraints or/and due to the measurement time limitation, the data are truncated [1]. Moreover, all the polarization cases of the scattered field are rarely measured in a multistatic configuration. The measurements are also ineluctably disturbed by noise, which does not a priori follow an uniform or a white Gaussian distribution [2]. It seems thus interesting to understand and analyze which measurements are the most relevant ones. The final goal is to reduce the number of experimental data points while guaranteeing the best reconstructions.

In this contribution, we focus our efforts on the polarization aspect. The polarization of the electromagnetic wave contains useful information as studies in radar polarimetry [3], [4], [5] or light scattering communities [6], [7] and references therein [8] point out. In inversion procedures, the different polarizations are generally considered to contain the same amount of information and hence, are treated as a whole. In fact, reconstruction results seem to be greatly influenced by the choice of the field components as shown by the results obtained in [9]. The present study is performed by calculating the amplitude scattering matrix using two classical polarization projections. The influence on the reconstruction results of each polarization projection will therefore be investigated. Moreover, in order to better apprehend the physical content associated to each term of the amplitude scattering matrix, we have decided to employ a simple induced current reconstruction algorithm which is rendered vectorial as the polarization states of the transmitter and the receiver are taken into account. The reconstructions are made on scaled models of aggregates [10] with experimental scattered fields acquired in the microwave frequency range [11]. These targets fulfill neither the Born or the Rytov approximation and thus only qualitative maps of the scene will be provided.

The paper is organized as follows. The scattered field is expressed in Part 2. Part 3 is devoted to the analysis of the available spectral information. In Part 4, amplitude scattering matrices are calculated using two conventions, the spherical convention often used in the microwave community and the Bohren and Huffman convention [12] often used in the light scattering community. The induced current reconstruction algorithm, which uses these amplitude scattering matrices as input is described in Part 5. The reconstruction results from the measurements are provided in Part 6 as well as the discussion on the impact of the polarization projection on the reconstructed target. Concluding remarks follow in Part 7.

* Corresponding author: christelle.eyraud@fresnel.fr

2. Far-field scattered field

The field scattered by a target, enclosed in a domain Ω and illuminated with a monochromatic electromagnetic wave, is calculated in a receiving zone Γ, at each receiver position $\mathbf{r} \in \Gamma$, by means of the observation equation which can be written as

$$\mathbf{E^s}(\mathbf{r}) = \int_\Omega \mathbf{G}(\mathbf{r},\mathbf{r}')\chi(\mathbf{r}')\mathbf{E}(\mathbf{r}')d\mathbf{r}' \qquad (1)$$

A free space configuration is considered, thus $\mathbf{G}$ is the dyadic free-space Green function between the object zone Ω and the receiver zone Γ. $\mathbf{E}$ and χ ($\chi(\mathbf{r}') = k(\mathbf{r}')^2 - k_0^2$) are respectively the field and the contrast in the Ω domain (with k_0 the wavenumber in vacuum and $k(\mathbf{r}')$ the wavenumber in zone Ω).

When the far-field conditions are realized [6], that is,

$$k_0 r \gg 1, \quad r \gg r', \quad \frac{k_0 r'}{2r} \gg 1, \quad \forall r \in \Gamma, \forall r' \in \Omega \qquad (2)$$

The dyadic free-space Green function in spherical coordinates (Figure 1(a)) can also be approximated by:

$$\mathbf{G}(\mathbf{r},\mathbf{r}') \approx \frac{e^{j\mathbf{k_s}.(\mathbf{r}-\mathbf{r}')}}{4\pi r}[\mathbf{I} - \mathbf{e}_r \otimes \mathbf{e}_r] \qquad (3)$$

where $\mathbf{k_s}$ is the scattered wavevector, $\mathbf{I}$ the identity operator, $\mathbf{a} \otimes \mathbf{b}$ the tensor product between the vector $\mathbf{a}$ and the vector $\mathbf{b}$ and ($\mathbf{e}_r$, $\mathbf{e}_\theta$, $\mathbf{e}_\phi$) are the unit vectors of the spherical basis.

3. Ewald sphere

If the transmitter and the receiver can be placed all around the Ω zone, on a sphere Γ of radius r, all the information in the far-field is reached for a considered frequency and the Ewald sphere is totally covered [13]. This Ewald sphere corresponds to the location, in the spectral domain, of the vector $\mathbf{K} = \mathbf{k_s} - \mathbf{k_i}$, where $\mathbf{k_i}$ (resp. $\mathbf{k_s}$) corresponds to the incident (resp. scattered) wavevector. Unfortunately this configuration is difficult to obtain in practical situations. Indeed, all geometrical positions may not be allowed due to various considerations (measurement time, mechanical constraints, ...).

Figure 1 describes the geometrical configuration associated to the experimental setup of the C.C.R.M. - Marseille employed in the present work for acquiring the data sets (see section 6.A). The origin O of the spherical coordinate system (r, θ, ϕ) is located at the center of the target zone Ω [14]. The transmitter is placed on the sphere surrounding the target, its position is described by (r^T, θ^T, ϕ^T) with $\theta^T \in [0, 2\pi]$ and $\phi^T \in [\phi_b^T, \phi_u^T]$ (where ϕ_b^T and ϕ_u^T are the limit ϕ^T-angles). The receiver, placed on the same sphere ($r^R = r^T$), has a position described by (r^R, θ^R, ϕ^R) with $\theta^R \in [\theta_b^R, \theta_u^R]$ (where θ_b^R and θ_u^R are the limit θ^R-angles) and with $\phi^R = 90°$. The associated Ewald sphere which describes the spectral information contained by the scattered field is represented in Figure 2. From a global point of view, this sphere is relatively well-filled. The lack of the backscattering zone - due to the limits of the θ^R angle - is balanced

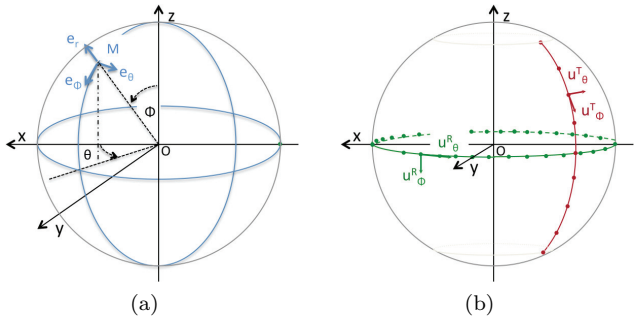

Fig. 1. Geometrical configuration.

by the variation of the θ^T angle between 0 and 2π. To take a closer look at this sphere, cross-sections defined at $k_x = 0$, $k_y = 0$ and $k_z = 0$ are presented in Figures 2(b), (c), (d). The plane $(k_x 0 k_y)$ is relatively well-filled. Nevertheless it can be noticed that it contains a larger amount of low spatial frequency values than of high frequency ones. In the $(k_x 0 k_z)$ and $(k_y 0 k_z)$ planes, parts of the disks are missing, i.e., the lower and the upper parts along the k_z-axis are truncated and only low spatial frequency values are present. This is due to the constrained measurement geometry, i.e., the angles between 0 and ϕ_b^T (30° in the case of Figure 2) are not accessible by the transmitter in the positive part of the z-axis and the angles between ϕ_u^T and π (50° in the case of the Figure 2) are excluded in the negative part. This explains also the asymmetry with respect to the $k_z = 0$ axis.

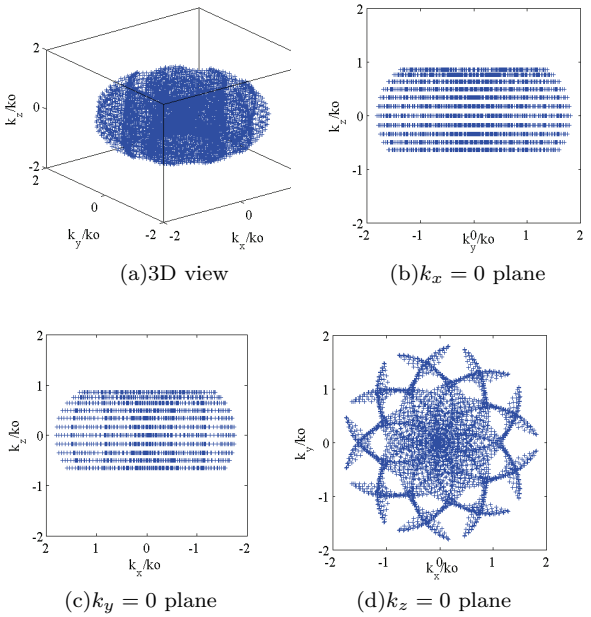

Fig. 2. Ewald sphere using the specified configuration with $\phi_b^T = 30°$, $\phi_u^T = 130°$, $\theta_b^R = \theta^T + 50°$ and $\theta_u^R = \theta^T + 310°$ (each point corresponds to a transmitter-receiver couple): (a) 3D visualization and (b), (c) and (d) cross-sections

In the following, the discussion on the polarization impact is restricted to this specific Ewald sphere topology.

4. Amplitude scattering matrix

In the far-field, for a non-absorbing medium, the complex amplitude scattering matrix $\mathbf{S}$, as defined in [6], describes the realtion between the components of the incident field vector and the components of the scattered field vector. With this definition, the scattered field vector $\mathbf{E^s}$ is linked to the incident field vector $\mathbf{E^i}$ as:

$$\mathbf{E^s} = \mathbf{S}\,\mathbf{E^i} \tag{4}$$

This scattering matrix is determined by the incidence and the scattering directions as well as by the properties of the target, but it also depends on the choice of the polarization basis. Two main conventions are usually used, the first one - called here the spherical convention - is well-spread in the microwave community while the second one - here called the Bohren and Huffman convention - is favored by the optics community.

4.A. Spherical convention

For a given transmitter/receiver couple, the scattering matrix can be constructed with a spherical convention, using as basis the ($\mathbf{u}_\theta^T$, $\mathbf{u}_\phi^T$) vectors for the incident wave and the ($\mathbf{u}_\theta^R$, $\mathbf{u}_\phi^R$) vectors for the scattered wave [15], [11] (Figures 1(b) and 3(a)). As the far-field conditions are assumed, the field vectors have no radial components and are then totally determined by their components along $\mathbf{u}_\theta^R$ and $\mathbf{u}_\phi^R$. Accordingly, the element $S_{p,q}$ of the scattering matrix corresponds to a scattered field measured along the $\mathbf{u}_q^R$ vector for an incident field $\mathbf{E^i}$ polarized along the $\mathbf{u}_p^T$ vector (for $p, q \in \{\phi, \theta\}$) and the scattering matrix is written as:

$$\begin{pmatrix} E_\theta^s \\ E_\phi^s \end{pmatrix} = \begin{pmatrix} S_{\theta\theta} & S_{\theta\phi} \\ S_{\phi\theta} & S_{\phi\phi} \end{pmatrix} \begin{pmatrix} E_\theta^i \\ E_\phi^i \end{pmatrix} \tag{5}$$

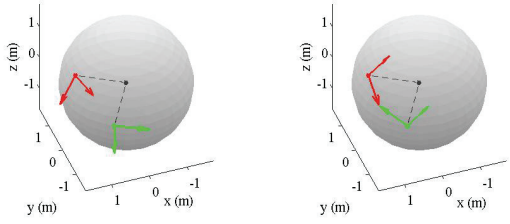

(a) (b)

Fig. 3. For a given couple of transmitter and receiver positions (source : $(r^T = 102\,\lambda, \theta^T = 100°, \phi^T = 60°)$, receiver $(r^R = 102\,\lambda, \theta^R = 150°, \phi^R = 90°)$, representation of the basis vectors for the source (red) and for the receiver (green) (the $\mathbf{k_i}$ and $\mathbf{k_s}$ vectors are plotted in black (- -)) under (a) the spherical convention, (b) the Bohren and Huffman convention.

This convention is particularly convenient when the fields are measured with several incident and scattering directions.

4.B. Bohren and Huffman convention

In the previous definition, the elements are not linked to the scattering plane, i.e, the plane containing both the $\mathbf{k}_i$ incident wave vector and the $\mathbf{k}_s$ scattered wave vector (see Figure 3(b)). For a given transmitter/receiver couple, the complex amplitude scattering matrix can be constructed using another basis related to this specific scattering plane, as proposed in the Bohren and Huffman (BH) definition [12] which is commonly used in the light scattering community. The scattered field components are then linked to the incident ones in the far-field region as follows:

$$\begin{pmatrix} E_\parallel^s \\ E_\perp^s \end{pmatrix} = \begin{pmatrix} S_{\parallel\parallel} & S_{\parallel\perp} \\ S_{\perp\parallel} & S_{\perp\perp} \end{pmatrix} \begin{pmatrix} E_\parallel^i \\ E_\perp^i \end{pmatrix} \tag{6}$$

where $E_\parallel$ (resp. $E_\perp$) corresponds to the field component parallel (resp. perpendicular) to the scattering plane and the element $S_{p,q}$ of the scattering matrix corresponds to a scattered field measured along the $\mathbf{u}_q^R$ vector for an incident field E^i polarized along the $\mathbf{u}_p^T$ vector (for $p, q \in \{\perp, \parallel\}$).

5. Induced current reconstructions based on scattering matrices

In a classical first-order diffraction tomography algorithm, the scattered field vector and the incident field are along the same direction and the Born approximation or the Rytov approximation is used in Equation (1). This equation becomes a scalar equation and the contrast map is then retrieved via an inverse Fourier transform (see for example [16], [17], [18]).

Here, a different approach is considered: (i) the entire vectorial nature of the fields is taken into account, and (ii) no linearized assumption is made. We only assume that the induced current vector $\mathbf{J}(\mathbf{r}') = \chi(\mathbf{r}')\,\mathbf{E}(\mathbf{r}')$ is collinear with the polarization state of the incident field $\mathbf{u}_p^T$ (for $p \in \{\phi, \theta, \perp, \parallel\}$). The scattered field expression becomes:

$$\mathbf{E^s}(\mathbf{r}) \approx \frac{e^{j\mathbf{k_s}.\mathbf{r}}}{4\pi r}\,[\mathbf{e}_\theta \otimes \mathbf{e}_\theta + \mathbf{e}_\phi \otimes \mathbf{e}_\phi]\mathbf{u}_p^T \int_\Omega e^{-j(\mathbf{k_s}-\mathbf{k_i}).\mathbf{r}'} J_p(\mathbf{r}') e^{-j\mathbf{k_i}.\mathbf{r}'} d\mathbf{r}' \tag{7}$$

The vector $\mathbf{u}_p^T$ describing the polarization state of the incident field is not constant for all the illumination directions. For a given choice of polarization ($p \in \{\theta, \phi, \perp, \parallel\}$), it can be written in the form

$$\mathbf{u}_p^T = f_p^r\,\mathbf{e}_r + f_p^\theta\,\mathbf{e}_\theta + f_p^\phi\,\mathbf{e}_\phi \tag{8}$$

where the terms $f_p^{r,\theta,\phi}$ are functions of the θ^T, ϕ^T, θ^R and ϕ^R angles. Due to the specific geometry of the configuration under investigation, the scattered field polarization vector is generally not collinear with the incident

field one. The vector $\mathbf{u}_q^R$, which represents the projection on the selected polarization ($q \in \{\theta, \phi, \perp, \|\}$) given by the receiver is:

$$\mathbf{u}_q^R = g_q^\theta \, \mathbf{e}_\theta + g_q^\phi \, \mathbf{e}_\phi \tag{9}$$

where the terms $g_q^{\theta,\phi}$ are functions of the θ^T, ϕ^T, θ^R and ϕ^R angles.
For a selected polarization case (p, q), the element of the scattering matrix $S_{p,q}$ (where $p \in \{\theta, \phi, \perp, \|\}$ and $q \in \{\theta, \phi, \perp, \|\}$) corresponds then to the scalar product between the vectors $\mathbf{u}_p^T$ and the vector $\mathbf{u}_q^R$:

$$\begin{aligned} S_{p,q} &= \mathbf{E^s}(\mathbf{r}).\mathbf{u}_q^R \\ &\approx \frac{e^{j\mathbf{k_s}.\mathbf{r}}}{4\pi r} \, \mathbf{u}_p^T.\mathbf{u}_q^R \int_\Omega e^{-j(\mathbf{k_s}-\mathbf{k_i}).\mathbf{r}'} J_p(\mathbf{r}') e^{-j\mathbf{k_i}.\mathbf{r}'} d\mathbf{r}' \end{aligned} \tag{10}$$

The magnitude of the induced current $|J_{p,q}|$ created by a target at the position $\mathbf{r}'$ - in a lossless embedding medium - is then linked to the measurement of the element $S_{p,q}$ of the scattering matrix by the following equation :

$$|J_{p,q}(\mathbf{r}')| \approx A \frac{|\widetilde{S_{p,q}}(\mathbf{K})|}{\mathbf{u}_p^T.\mathbf{u}_q^R}, \quad \text{if } \mathbf{u}_p^T.\mathbf{u}_q^R \neq 0 \tag{11}$$

where $1/A = |\frac{e^{j\mathbf{k_s}.\mathbf{r}}}{4\pi r}|$ is a constant term and $\widetilde{S_{p,q}}(\mathbf{K})$ is the 3D inverse Fourier transform of $S_{p,q}(\mathbf{r}')$.

In this work, we only use measurement points with collinear incident and scattered polarization vectors. The $S_{\theta\phi}$, $S_{\|\perp}$ and $S_{\perp\|}$ elements are thus not exploited herein as they correspond to situations where the incident and the scattered polarization vectors are orthogonal. Nevertheless, these elements are non null only when the target is changing the polarization of the impinging wave. Finally, the number of elements in the complex amplitude scattering matrix which will be considered in the imaging algorithm may vary according to the polarization state. Table 1 summarizes the percent of measurements used in each case.

Table 1. Measurements used with the inversion procedure for the configuration with $\phi_b^T = 30°$, $\phi_u^T = 130°$, $\theta_b^R = 50°$ and $\theta_u^R = 310°$

Polarization	$S_{\phi\phi}$	$S_{\theta\theta}$	$S_{\phi\theta}$	$S_{\perp\perp}$	$S_{\|\|}$
%	84	55	33	100	46
Number	4407	2886	1732	5247	2414

6. Reconstruction results from measurements

In this part, the induced current reconstruction algorithm is assessed using scattering matrices determined from experimental data.

6.A. Experimental configuration

To get all possible information on an object in the far-field, the field should be measured on the entire sphere enclosing the target. The spherical experimental setup in the anechoic chamber of the C.C.R.M. - Marseille allows to obtain a configuration similar to the one described in Figure 1. This setup has been used by the researchers of the Institut Fresnel to perform the measurements.

6.A.1. Geometrical arrangement

For a target at the origin of the coordinate system of the spherical setup (Figure 4), the scattered field can be measured on a portion of the sphere enclosing this object. Indeed, the transmitting antenna can move on

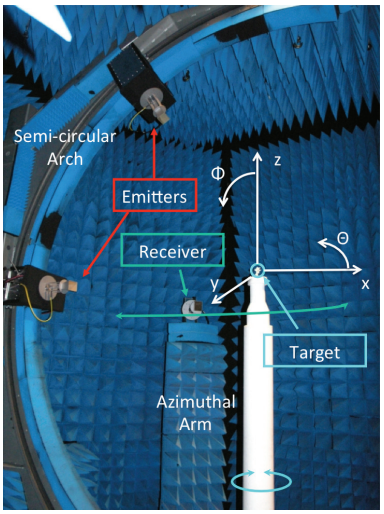

Fig. 4. Experimental setup: photography of the anechoic chamber.

a circular arch, the target can rotate around the $z-$axis - which allows to create a situation which is similar to a fixed target and a source displaced over several vertical arches around the target. The receiver is also moved in the horizontal plane with a circular movement centered on the target. This setup was already described in several publications (see for example [19]). As the distance between the center of the setup and the transmitting antenna or the receiving antenna is 102 λ, we are in agreement with the far-field conditions (equation (2)) as long as the radius of the minimum sphere enclosing the target has a diameter smaller than 10 λ.

6.A.2. Experimental parameters

The geometrical parameters are chosen in agreement with the maximum spatial bandwidth of the scattered field to measure the field in a non-redundant way [1]. Indeed, 99 positions of the source are used in this study. Each source has a position (r^T, θ^T, ϕ^T) where $\phi^T \in [\phi_b^T = 30° : 10 : \phi_u^T = 130°]$ and $\theta^T \in [\theta_b^T = 20° : 40 : \theta_u^T = 340°]$. The field is measured at 53 receiver positions $(r^R, \theta^R, \phi^R = 90°)$ where $\theta^R \in [\theta_b^R = \theta^T + 50° : 5 : \theta_u^R = \theta^T + 310°]$. The measurements were performed for a wavelength comprised between $\lambda = 15\,\text{mm}$ and $\lambda = 18.7\,\text{mm}$, but all the results here are for $\lambda = 16.7\,\text{mm}$. Measurements are calibrated to refer to the scattered field associated to an incident field

having a unit magnitude and a null phase at the center of the setup [20], [21]. Data processing is required to extract the maximum of information [2] from the measurements. In particular all the fields are processed to avoid drift phenomena [22].

6.A.3. Polarization

As the two antennas are linearly polarized pyramidal horns (ARAMWH-1826B), the target is illuminated with a linearly polarized wave and one single polarization component of the scattered field is measured at each measurement point. The different polarization cases are obtained by combining two different emitting antennas plus a rotation of the receiving antenna. The experimental data are thus obtained by measuring for each incident field parallel to $\mathbf{u}_\phi^T$ (and then $\mathbf{u}_\theta^T$), the scattered field vectors which are parallel to $\mathbf{u}_\phi^R$ and to $\mathbf{u}_\theta^R$ (see Figure 1 for notations).

6.B. Targets

We have considered two targets which are clusters of spheres. The spheres of the first object have diameters which are comparable to the wavelength and in theory it should be possible to separate them with our algorithm. On the contrary, the spheres of the second object are much smaller and can not easily be separated with such an algorithm.

The first target is a pyramid of four $1.5\,\lambda$ in diameter spheres of PMMA ($\varepsilon_r = 2.6$) (Figure 5(a)). Its total size is equal to $3\,\lambda$. It has a density of approximatively 50% as compared to its minimum covering sphere. The second target is an horizontal shaped aggregate composed of 74 spheres (Figure 5(b)). This object was made by stereo lithography, which is a sequential deposit of layers of liquid acrylate resin ($\varepsilon_r = 2.85 + j0.06$) [10]. The diameter of each sphere is equal to $0.3\,\lambda$. Its total size is equal to $5\,\lambda$. It has a density of approximatevely 3% as compared to its minimum covering sphere.

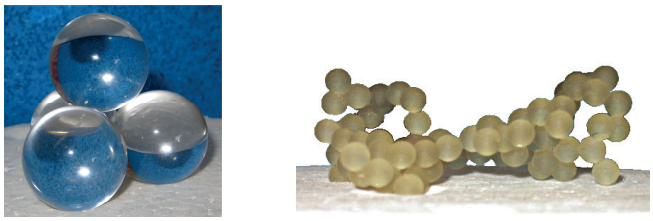

(a) (b)

Fig. 5. Dielectric targets: (a) Pyramid of 4 spheres (sphere diameter: $1.5\,\lambda$) and (b) Aggregate of 74 spheres (sphere diameter: $0.3\,\lambda$)

Due to their size and their permittivity contrast with respect to the background, the two targets do not fullfil the validity condition of the Born or the Rytov approximation [23].

6.C. Reconstruction parameters

6.C.1. Investigation zone

The dimension of the investigation zone is directly linked to the discretisation step in the spectral domain. As the scattered field is not measured with an uniform step along each component of $\mathbf{K}$, the field has to be interpolated before performing the inverse Fourier transform. For the present measurement configuration, the spectral domain step is set equal to 2 leading to an associated investigation zone corresponding to a cube with a side length of $30\,\lambda$. As the voxel width in the reconstructed map is directly linked to the maximum values in the spectral domain, the voxel width is bigger along the z-axis ($0.65\,\lambda$) than along the y-axis ($0.27\,\lambda$) and along the x-axis ($0.28\,\lambda$).

6.C.2. Normalized maps

Each reconstructed map contains qualitative information - position and shape - on the target. We only consider magnitude maps and normalize them to obtain values between 0 and 1. A normalized map M_n is thus obtained from an initial map M with

$$M_n = \frac{|M| - min(|M|)}{max(|M|) - min(|M|)} \tag{12}$$

6.C.3. Estimate assessment

To have a quantitative assessment of the reconstruction, we use three criteria. Before calculating these criteria, it is necessary to determined the real position of the target mass center $\mathbf{d}^* = (x_d, y_d, z_d)$ to avoid bias. Using the reconstructed maps, we determined the real position of this target mass center using a 3D cross correlation between the reconstructed map and the expected one as explained in [9]. The first criterion is a comparison between the true and reconstructed normalized maps using a classical L_2 norm.

$$C^{L_2} = ||M_n^{true} - M_n^{reco}||_{L_2} \tag{13}$$

We have shown in [9] that the usually adopted criteria L_1 and L_2-norms are not very well suited to evaluate the accuracy of the reconstruction of complex targets as their values are particularly dependent on the reconstruction of the empty voxels. We thus use two other criteria, i.e., the correlation C^c and the cross correlation C^{cc} coefficients between the two maps:

$$C^c = \frac{Cov(M_n^{reco}, M_n^{true})}{\sqrt{Var(M_n^{reco})\,Var(M_n^{true})}} \tag{14}$$

$$C^{cc} = \frac{\sum_{\mathbf{r}}(M_n^{true}(\mathbf{r}+\mathbf{d}^*))\overline{(M_n^{reco}(\mathbf{d}^*))}}{\sum_{\mathbf{r}}(M_n^{true}(\mathbf{r}+\mathbf{0}))\overline{(M_n^{true}(\mathbf{0}))}} \tag{15}$$

where $Cov(u,v)$ is the covariance between u and v, $Var(u)$ the variance of u, $\mathbf{r}$ the position of the considered cell and $\mathbf{d}^*$ the real position of the target determined as explained in the following. The C^{cc} coefficient quantifies the similarity between the two maps by only comparing the voxels containing some material. The more similar

the two maps are, the closer to 0 the criteria C^{L_2} is and the closer to 1 the criteria C^{cc} and C^{c} are. These criteria are calculated considering a reduced $(6 \times 6 \times 6)\lambda^3$ cubic investigation zone centered at $\mathbf{0}$. Indeed, due to the relative number of voxels without material in the calculation, the considered zone dimension affects the C^{L_2} criterion.

6.D. Reconstructions in the different polarization cases

In this part, results are presented and then discussed.

6.D.1. Pyramid of spheres

The true position of the center of gravity of the target was found to be at $d^* = (0.12, 0.12, 0.68)\,\lambda$. This position is very close to the expected one $(0, 0, 0.68)\,\lambda$.

The reconstructions using the amplitude scattering matrix and the spherical convention are plotted in Figures 6, 8 and 7. In each polarization case, the presence of the target can be seen and its size can be determined on these maps. Nevertheless, the quality of the imaging results is strongly different from a chosen polarization case to another. The $\phi\phi$ and $\phi\theta$ cases allow to obtain rather good results, while the $\theta\theta$ case is clearly less accurate. The kind of information contained in each reconstruction is also different according to the polarization cases. Indeed with the $S_{\phi\phi}$ element, the boundaries of the spheres are better reconstructed than the internal parts. On the contrary, with the $S_{\phi\theta}$ element, the internal parts of the spheres are better reconstructed than the boundaries. Looking at the criteria values, the L_2 criterion gives very little information as this criterion is the same (equal to 0.002) for all polarization cases. The values of the two other criteria are given in Table 2. The C^{c} and C^{cc} criteria show that the best cases are the $\phi\phi$ and $\phi\theta$ cases, the latter being slightly better due to the good reconstruction of the internal part of the spheres.

Let us now consider the reconstruction obtained with the scattering matrix elements under the Bohren and Huffman definition (Figures 9 and 10). The reconstruction with the $S_{\perp\perp}$ element is very close to the one obtained with the $S_{\phi\phi}$ element. This is confirmed by the C^{cc} and C^{c} criteria (Table 2). The result with the $S_{\parallel\parallel}$ element is not very good and is similar to the one obtained with the $S_{\theta\theta}$ element.

Table 2. Criteria values for the pyramid of spheres.

	$S_{\phi\phi}$	$S_{\theta\theta}$	$S_{\phi\theta}$	$S_{\perp\perp}$	$S_{\parallel\parallel}$
C^{cc}	0.47	0.27	0.53	0.46	0.28
C^{c}	0.73	0.68	0.71	0.72	0.72

6.D.2. Aggregate of spheres

The real position of the aggregate mass center using the correlation criterion was found at $(0, 0.18, 0.31)\,\lambda$ and the expected position was $(0, 0, 0.41)\,\lambda$. This target is a "flat" target, i.e, it has a small thickness along the z-axis as it can be seen in Figure 11. The reconstruction

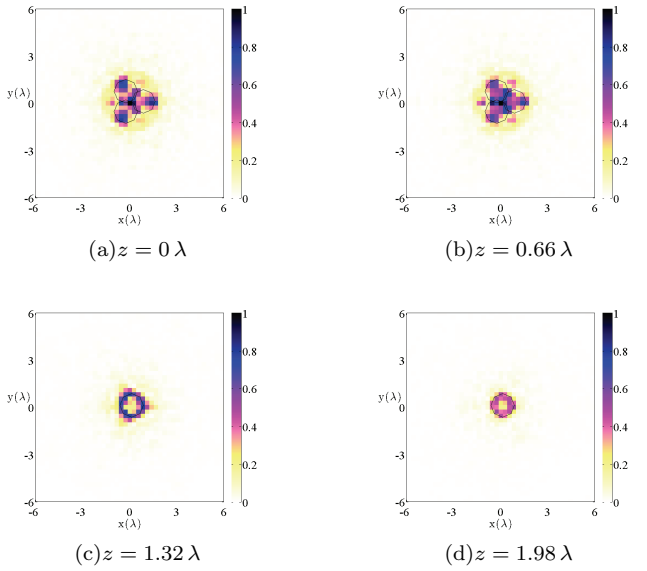

Fig. 6. Maps reconstructed at several altitudes using the pyramid of spheres scattered fields in the $S_{\phi\phi}$ polarization. The real sphere boundaries are plotted in black.

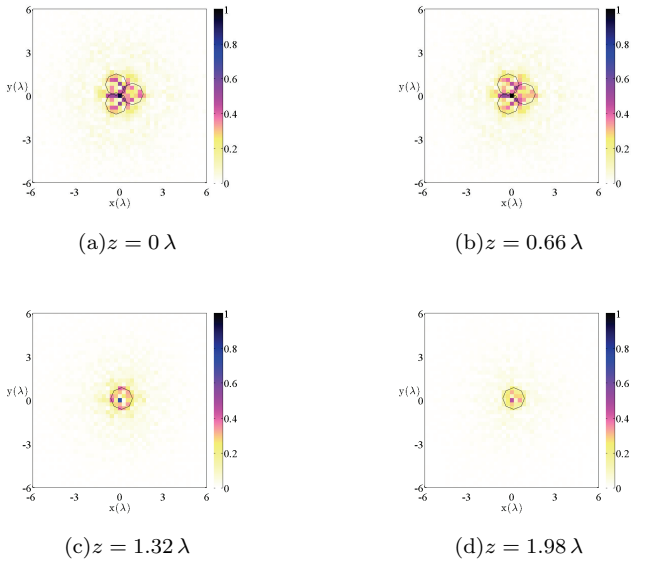

Fig. 7. Maps reconstructed at several altitudes using the pyramid of spheres scattered fields in the $S_{\theta\theta}$ polarization. The real spheres boundaries are plotted in black.

results are plotted at the altitude $z = 0$ for the different polarization cases in Figures 12 - 13 and the criteria values are given in Table 3. The localization and the object global dimensions are well determined for all the polarization cases. As expected, none of the cases allows to distinguish the spheres due to the use of a linear imaging algorithm. In the same way as for the previous object, the reconstruction results differ from a polariza-

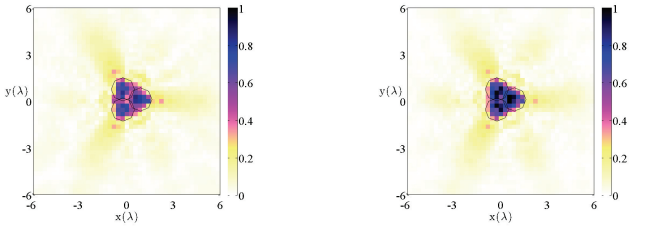

(a)$z = 0\,\lambda$ (b)$z = 0.66\,\lambda$

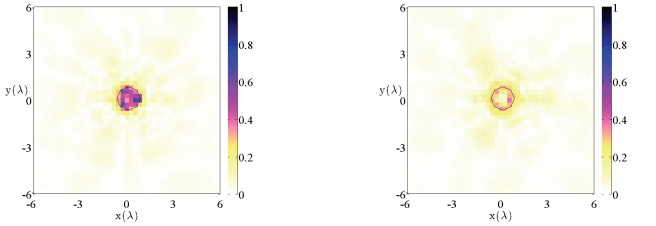

(c)$z = 1.32\,\lambda$ (d)$z = 1.98\,\lambda$

Fig. 8. Maps reconstructed at several altitudes using the pyramid of spheres scattered fields in the $S_{\phi\theta}$ polarization. The real spheres boundaries are plotted in black.

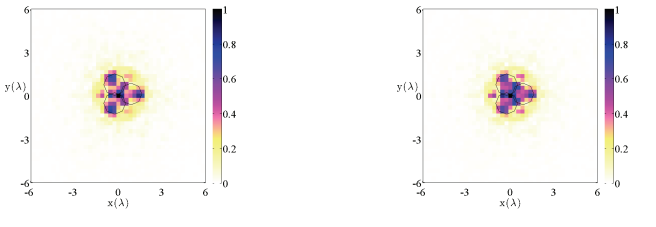

(a)$z = 0\,\lambda$ (b)$z = 0.66\,\lambda$

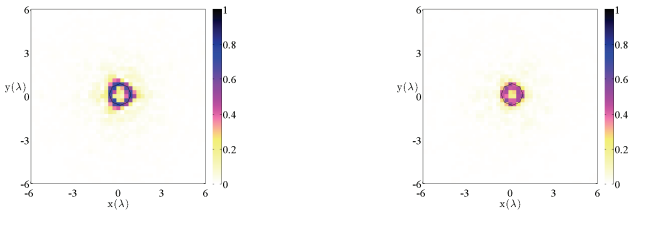

(c)$z = 1.32\,\lambda$ (d)$z = 1.98\,\lambda$

Fig. 9. Maps reconstructed at several altitudes using the pyramid of spheres scattered fields in the $S_{\perp\perp}$ element. The real spheres boundaries are plotted in black.

tion case to another. Indeed, the reconstruction in the $\theta\theta$ case is the worst according to the C^c and C^{cc} criteria. The imaging results obtained with the $S_{\phi\phi}$ and $S_{\perp\perp}$ elements are very similar - it is also confirmed by the criteria values - and all the "branches" of the target are reconstructed in these cases. The $S_{\parallel\parallel}$ element provides a better reconstruction than the $S_{\theta\theta}$ element, where all the "branches" of the target are reconstructed,

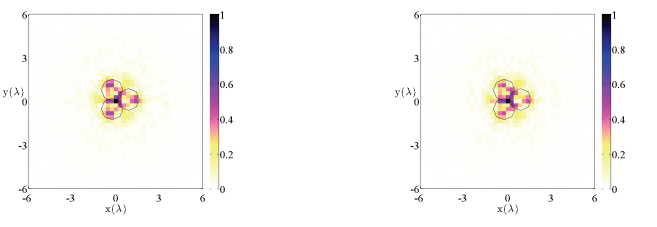

(a)$z = 0\,\lambda$ (b)$z = 0.66\,\lambda$

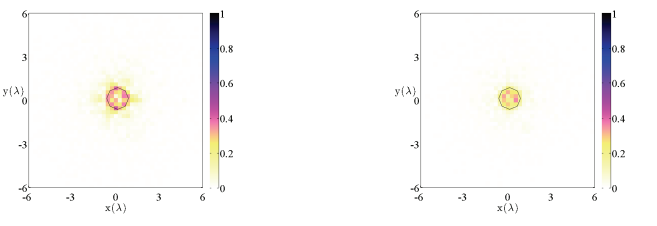

(c)$z = 1.32\,\lambda$ (d)$z = 1.98\,\lambda$

Fig. 10. Maps reconstructed at several altitudes using the pyramid of spheres scattered fields in the $S_{\parallel\parallel}$ element. The real spheres boundaries are plotted in black.

but the boundaries of the reconstruction are blurred. In the $S_{\phi\theta}$ reconstruction result, some "branches" are missing and this leads to lower criteria values, but the others "branches" are correctly reconstructed.

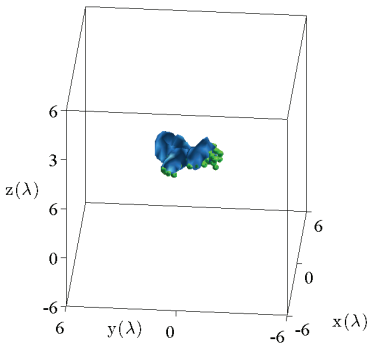

Fig. 11. 3D visualization (in blue) of the reconstructed maps using the $S_{\perp\perp}$ case - the iso-surface threshold value is set to 0.2. The real 74 sphere aggregate is overlaid (in green).

Table 3. Criteria values for the aggregate.

	$S_{\phi\phi}$	$S_{\theta\theta}$	$S_{\phi\theta}$	$S_{\perp\perp}$	$S_{\parallel\parallel}$
L_2	0.009	0.008	0.014	0.008	0.009
C^{cc}	0.70	0.58	0.62	0.70	0.67
C^c	0.51	0.47	0.40	0.51	0.50

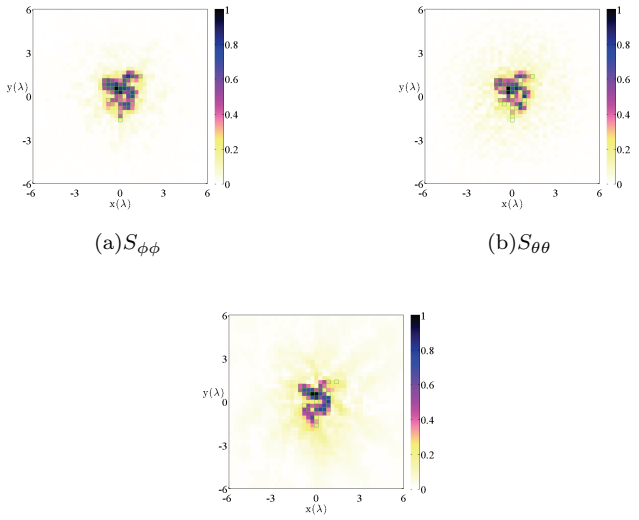

(a)$S_{\phi\phi}$ (b)$S_{\theta\theta}$

(c)$S_{\phi\theta}$

Fig. 12. Maps reconstructed at $z = 0\,\lambda$ using different elements of the scattered fields matrix with the spherical convention. The real aggregate boundaries are plotted in green.

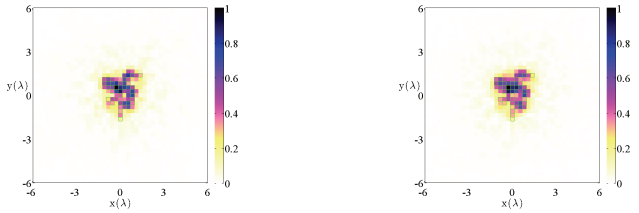

(a)$S_{\perp\perp}$ (b)$S_{\parallel\parallel}$

Fig. 13. Maps reconstructed at $z = 0\,\lambda$ using different elements of the scattered fields matrix with the Bohren and Huffman convention. The real aggregate boundaries are plotted in green.

6.D.3. Discussion

For the two targets, the reconstructions from the $S_{\phi\phi}$ and the $S_{\phi\theta}$ elements are rather close to the real object and the reconstructions from the $S_{\theta\theta}$ element is clearly less accurate. With the Bohren and Huffman polarization definition, the $S_{\perp\perp}$ element leads to better results than the $S_{\parallel\parallel}$ element. The results from the $S_{\perp\perp}$ case are similar to the ones derived from the $S_{\phi\phi}$ case. Nevertheless, it can be noticed that the $S_{\perp\perp}$ element is the only one taking into account all the measurements and this can be of interest depending on the target under test.

The different parts of the target are not reconstructed in a similar way from one polarization case to another even if the polarization of the incident wave is the same. This is clearly visible while comparing the reconstructions from the $S_{\phi\phi}$ and the $S_{\phi\theta}$ cases for the two targets. To better understand this behavior, we have plotted the magnitude of the mean of the induced currents calculated in the target zone at the altitude $z = 0.45\,\lambda$ (Figure 14) - corresponding to the middle of the three spheres of lower altitude - for the pyramid of spheres. These currents were obtained using a volume integral algorithm [24], for source positions between $\phi^T = 30°$ and $\phi^T = 120°$ with a 30° step, considering all the θ^T angles, and for a single transmitter polarization $\mathbf{u}_\phi^T$. We can see that the magnitudes of the components along $\mathbf{e}_x$ and $\mathbf{e}_y$ have stronger values in the central part of the spheres than on the boundaries, in opposition to the components along $\mathbf{e}_z$ which have an inverse behavior. Thus, the projection of the resulting scattered field along $\mathbf{u}_\phi^R$ or $\mathbf{u}_\theta^R$ will provide a different informative content. These maps consolidate the results shown in Figures 6 and 8, where different parts of the target were reconstructed according to the chosen polarization reception orientation.

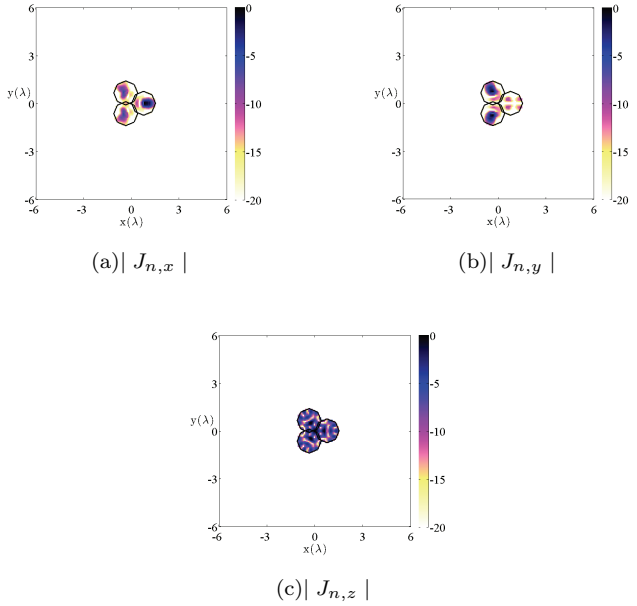

(a)$\mid J_{n,x} \mid$ (b)$\mid J_{n,y} \mid$

(c)$\mid J_{n,z} \mid$

Fig. 14. Maps of the normalized induced current magnitude in the target zone at altitude $z = 0.45\,\lambda$ for the pyramid of spheres for a transmitter polarization choice along $\mathbf{e}_\phi$. $J_{n,i}$ corresponds to the component along the $\mathbf{e}_i$ vector ($i \in \{x, y, z\}$).

7. Conclusion

In this paper, we have considered the amplitude scattering matrix calculated with two classical polarization projections. The same imaging procedure, a vectorial induced current reconstruction algorithm, has then been used, while the input components varied according to the projections choices.

Our imaging process was tested using the amplitude scattering matrix calculated from experimental fields measured in an anechoic chamber for two clusters of spheres, a pyramid of 4 spheres with a radius of $0.75\,\lambda$

and an aggregate of 74 spheres with a radius of $0.15\,\lambda$. The results show that the polarization choice has a strong influence on the imaging result. With a spherical configuration, the $S_{\perp\perp}$ element using the *Bohren and Huffman* convention or the $S_{\phi\phi}$ and $S_{\phi\theta}$ elements using the *spherical* convention lead to the best results. A suitable choice of polarization will therefore provide different kinds of information contents, in particular the capability to focus on either the inner or the outer details of the target substructure.

In our linear algorithm, far-field conditions are required and the induced current vector is assumed to be collinear with the incident field polarization vector. Under these assumptions, three-dimensional qualitative maps of the scene are retrieved in real-time with a low-memory requirement. Depending on the studied target, in particular if the target can create strong depolarization effects, it might be of interest to pursue the investigation with a non-linear imaging algorithm.

References

[1] O. Bucci and T. Isernia, "Electromagnetic inverse scattering: retrievable information and measurement strategies", Radio Science, **32**, 2123–2137 (1997).

[2] J.-M. Geffrin, C. Eyraud, A. Litman and P. Sabouroux, "Optimization of a Bistatic Microwave Scattering Measurement Setup: From High to Low Scattering Targets", Radio Science, **44**, RS2007 (2009).

[3] S. Cloude and E. Pottier, "A review of target decomposition theorems in radar polarimetry", IEEE Trans. Geosci. Remote Sens. **34**, 498–518 (1996).

[4] A. Roueff, A. Arnaubec, P.-C. Dubois-Fernandez and Ph. Refregier, "Cramer-Rao lower bound analysis of vegetation height estimation with random volume over ground model and polarimetric SAR interferometry", IEEE Geosci. Remote Sens. Lett. **8**, 1115–1119 (2011).

[5] S. Bellez, H. Roussel, C. Dahon, J. Castelli and A. Cheraly, "A Full Polarimetric Bistatic Radar Imaging Experiments on Sets of Dielectric Cylinders Above a Conductive Circular Plate", IEEE Trans. Geosci. Remote Sens. **99**, 1–13 (2013).

[6] M. Mishchenko, L. Travis and A. Lacis, "Scattering, Absorption, and Emission of Light by Small Particles", Cambridge University Press (2002).

[7] O. Merchiers, C. Eyraud, J.-M. Geffrin, R. Vaillon, B. Stout, P. Sabouroux and B. Lacroix, "Microwave measurements of the full amplitude scattering matrix of a complex aggregate: a database for the assessment of light scattering codes", Opt. Express **18**, 12119 (2010).

[8] G. Videen, Y. Yatskiv and M. Mishchenko, "Photopolarimetry in Remote Sensing", Proc. NATO Advanced Study Institute **161** (2003).

[9] C. Eyraud, J.-M. Geffrin and A. Litman, "3D-aggregate quantitative imaging: experimental results and polarization effects", IEEE Trans. Antennas Propag. **59**, 1237–1244 (2011).

[10] R. Vaillon, J-M. Geffrin, C. Eyraud, O. Merchiers, P. Sabouroux and B. Lacroix, "A new implementation of a microwave analog to light scattering measuremen device", J. Quant. Spectrosc. Radiat. Transf. **112**, 1753–1760 (2011).

[11] O. Merchiers, J.-M. Geffrin, R. Vaillon, P. Sabouroux and B. Lacroix, "Microwave analog to light scattering measurements on a fully characterized complex aggregate", Appl. Phys. Lett. **94**, 181107 (2009).

[12] G. Bohren and D. Huffman, "Absorption and Scattering of Light by Small Particles", John Wiley and Sons (1983).

[13] A. Kak and M. Slaney, "Principles of Computerized Tomographic Imaging", Society of Industrial and Applied Mathematics (2001).

[14] D. Zwillinger, "CRC Standard Mathematical Tables and Formulae", Chapman and Hall (2002).

[15] M. Michshenko, "Calculation of the amplitude matrix for a nonspherical particle in a fixed orientation", Appl. Opt. **39**, 1026–1031 (2000).

[16] Sung, W. Choi, C. Fang-Yen, K. Badizadegan, R. Dasari and M. Feld, "Optical diffraction tomography for high resolution live cell imaging", Opt. Express **17**, 266–277 (2009).

[17] G. Gurg and E. Wolf, "Relation between computed tomography and diffraction tomography", J. Opt. Soc. Am. A **18**, 2132–2137 (2001).

[18] A. Devaney, "Mathematical foundations of imaging, tomography and wavefield inversion", Cambridge University Press, (2012).

[19] J.-M. Geffrin and P. Sabouroux, "Continuing with the Fresnel database: Experimental setup and improvements in 3D scattering measurements", Inverse Probl., **25**, 024001 (2009).

[20] P.M. van den Berg, M.G. Coté, and R.E. Kleinman, "Blind shape reconstruction from experimental data", IEEE Trans. Antennas Propagat., **43**, 1389–1396 (1995).

[21] C. Eyraud, J.-M. Geffrin, P. Sabouroux, P.C. Chaumet, H. Tortel, H. Giovannini and A. Litman, "Validation of a 3D bistatic microwave scattering measurement setup", Radio Science, **43**, RS4018 (2008).

[22] C. Eyraud, J.-M. Geffrin, A. Litman, P. Sabouroux, and H. Giovannini, "Drift correction for scattering measurements", Appl. Phys. Lett., **89**, 244104 (2006).

[23] W. Wang, J. Li and F. Niu, "A revisit to the validity of Born approximation in high frequency scattering problems", Microwave Opt. Tech. Lett., **54**, 2792–2797, (2012).

[24] C. Eyraud, A. Litman, A. Hérique, and W. Kofman, "Microwave imaging from experimental data within a Bayesian framework with realistic random noise", Inverse Probl., **25**, 024005 (2009).